ACADEMIC PRESS

Available online at www.sciencedirect.com

SCIENCE DIRECT®

Journal of Computational Physics 184 (2003) 244–265

JOURNAL OF COMPUTATIONAL PHYSICS

www.elsevier.com/locate/jcp

A finite volume code for meridional circulation in stars

Suzanne Talon*, Alain Vincent, Georges Michaud, Jacques Richer

Département de Physique, Université de Montréal, Montréal Canada PQ H3C 3J7
CERCA, 5160 boul. Décarie, Montréal Canada PQ H3X 2H9

Received 29 May 2002; received in revised form 7 October 2002; accepted 14 October 2002

Abstract

To understand the driving of both meridional circulation and differential rotation in radiative envelopes of stars, one has to solve for 3D mass, momentum, and energy conservation equations for a compressible gas in a central gravity field. In this study, we propose a novel finite volume technique that uses Cartesian geometry thus reducing greatly the complexity of spherical operators. The boundary conditions are efficiently imposed at the surface of the star using the fictitious points technique. We use the anelastic approximation and the Poisson equation for pressure is solved by the Jacobi method which preserves natural symmetries. We present analytical test cases of the fictitious domain technique, and show our results of asymptotic circulation in a model with little stratification and a large viscosity.

1. Introduction

Stellar astrophysics often has to consider matter in a state which is far from conditions that can be reproduced on earth (extreme temperatures and pressures for example). As far as stellar hydrodynamics is concerned, a process which has received a lot of attention from numerical studies is convection (see e.g. [46]), where excessively large Rayleigh numbers can be encountered ($R_T \gg 10^{20}$). Since the early works dating back to the mid-70s [17,26], both 2D and 3D studies have been performed by several authors (e.g. [11,13,34,38,47] and references therein) and new phenomena usually appeared when an order of magnitude was gained in terms of Rayleigh number. Some attention was also given to more local studies of magneto-hydrodynamics (see e.g. [3,31,54]).

Even in stellar regions which are convectively stable, hydrodynamical processes must be present: shear instabilities can occur in differentially rotating stars [5,14,45,61], gravity waves should appear below and above convective regions [39], baroclinic instabilities may appear in several locations [16,19,25]. These are of major importance to stellar models since redistribution of chemicals within the star greatly affects its

* Corresponding author. Tel.: +1-514-369-5234; fax: +1-514-369-3880.
E-mail addresses: talon@cerca.umontreal.ca (S. Talon), vincent@cerca.umontreal.ca (A. Vincent), michaudg@cerca.umontreal.ca (G. Michaud), jacques.richer@umontreal.ca (J. Richer).

0021-9991/02/$ - see front matter
PII: S0021-9991(02)00029-3

subsequent evolution (see e.g. [43]). Here, we will concentrate on the "meridional circulation" in rotating stars [12,59], which to our knowledge, only Clement [9] has attempted to model numerically in 2 or 3 dimensions.

Several authors tackled the problem of finding the exact *shape* of the circulation pattern for a given rotation state [12,33,41,42,44,48,51,59], while others emphasized the *effect* of meridional circulation mainly as a source of chemical mixing [7,29,30,49,62]. However, none of these fully took into account freely developing 3D movements, thus neglecting many features of the hydrodynamical processes involved. Kippenhahn [23] suggested that, when viscosity is lowered, an equilibrium circulation could not be reached and that the resulting pattern would resemble more closely that of a *random circulation*, involving small scale structures, a result criticized by Tassoul and Tassoul [52].

Meridional circulation actually arises from the mismatch between heat transport, which naturally tends towards spherically symmetric, and the ellipsoidal structure of a rotating star [58]. In this problem, geometry is thus of utmost importance in order to satisfactorily represent reality. Furthermore, the discretization of the computational domain should be able to cope with a non-spherical stellar surface which depends on the distribution of angular momentum.

Cartesian grid methods are nowadays gaining in popularity (see [60] and references therein). Indeed, they have the great advantage of using a simple structured grid, thus avoiding all the problems associated with the generation and maintenance of body-conforming unstructured grids. Furthermore, the numerical equations obtained retain their standard formulation. The challenge is then to properly enforce the boundary conditions.

Several techniques have been developed, each presenting its own advantages; the contour method, in which the interface is "diffuse" and followed through the resolution of an advection equation (e.g. [1]), flux limiter for finite volume methods which are appropriate for Neumann type conditions (e.g. [6]) or sharp interface methods (e.g. [57]). Mask methods have also been developed in order to allow the use of simple spectral algorithms in arbitrary domains (e.g. [4]). In this paper, we will describe a fictitious boundary technique, designed to allow preservation of the natural symmetries of the problem.

In Section 2, we present the time-dependent 3D anelastic compressible equations of our problem. We then describe in Section 3 how to use fictitious points to represent the star's surface using a Cartesian coordinate system in spite of the stellar model ellipsoidal shape. The method is tested by solving the Poisson equation in spherical geometry. Section 4 describes the discretization of the equations and a novel fourth-order finite volume algorithm to solve them. Finally, in Section 5 we validate our approach by presenting test cases of meridional circulation.

2. System of equations and geometry

We would like to solve the problem of thermal imbalance in rotating stars from first principles. We thus begin our discussion with the full Navier–Stokes equations, expressing the conservation of mass

$$\frac{\partial \rho}{\partial t} + \vec{\nabla} \cdot \left(\rho \vec{w} \right) = 0, \tag{1}$$

where ρ is the density and w the velocity in the rotating reference frame, and of momentum

$$\frac{\partial \left(\rho \vec{w} \right)}{\partial t} + \vec{\nabla} \cdot \left(\rho \vec{w} \vec{w} + P \overline{\overline{I}} - \overline{\overline{\tau}} \right) = \rho \vec{g} - 2\rho \vec{\Omega} \times \vec{w} - \rho \vec{\Omega} \times \left(\vec{\Omega} \times \vec{r} \right) = \rho \vec{g}_{\text{eff}} - 2\rho \vec{\Omega} \times \vec{w}, \tag{2}$$

where $\vec{w}\vec{w}$ is the velocity dyad, P is the pressure, $\overline{\overline{I}}$ the identity tensor, $\overline{\overline{\tau}}$ the viscous tensor, $\vec{g}$ the local gravitational acceleration, $\vec{\Omega} = \Omega \vec{e}_z$ the rotation velocity of the reference frame and $\vec{g}_{\text{eff}}$ is the effective

gravity (which takes into account the centrifugal acceleration). Those equations are written in a rotating frame of reference and the total velocity $\vec{u}$ is expressed by

$$\vec{u} = \vec{\Omega} \times \vec{r} + \vec{w} \tag{3}$$

($\vec{\Omega}$ is also the star's initial, solid body, angular velocity).

The next equation, namely that of energy, is of utmost importance. Indeed, it is the thermal imbalance of the rotating star which is the driving term here [12,59], and that must be incorporated with great care in the code. This imbalance has generally been expressed analytically in terms of specific entropy s [12,33,48,51,59,62], and it is the formulation we will be using here

$$\rho T \frac{\partial s}{\partial t} + \rho T \vec{\nabla} s \cdot \vec{w} = \left(\bar{\bar{\tau}} \cdot \vec{\nabla} \right) \cdot \vec{w} + \vec{\nabla} \cdot \left(\chi \vec{\nabla} T \right), \tag{4}$$

where T is the temperature and χ, the thermal conductivity.

The equation for the evolution of momentum includes the viscous tensor

$$\tau_{ij} = \rho v \left[\left(\partial_i w_j + \partial_j w_i \right) - \frac{2}{3} \left(\vec{\nabla} \cdot \vec{w} \right) \delta_{ij} \right], \tag{5}$$

assuming a Newtonian fluid. Furthermore, closure of the system of equations requires an equation of state

$$P = \frac{\mathscr{R}}{\mu} \rho T, \tag{6}$$

where $\mathscr{R} = 8.31 \times 10^7 \mathrm{erg/K/g}$ is the universal gas constant and μ, the mean molecular weight, as well as a relation between entropy and other state variables

$$s = c_\mathrm{p} \ln \left(\frac{T}{P^{2/5}} \right), \tag{7}$$

where c_p is the specific heat. This relation is strictly valid up to an additive constant and for a monatomic perfect gas.

2.1. Time-scales and typical stellar values

Estimates of typical stellar values for the simulation's main physical parameters are given in Table 1. They correspond to conditions in the radiative region of a 2.2 solar mass star [8]; in such a model only the inner 10% in radius is convective, the rest being in radiative equilibrium.

There are a number of time-scales associated with the physical processes to be described:

- *Dynamical time-scale*. The dynamical (or free-fall) time-scale is the typical time over which a (dynamically stable) star reacts, via pressure waves, to a perturbation of its hydrostatic equilibrium. It is calculated using the free-fall time of a particle over a distance R in a (constant) gravity field of magnitude g_s

$$t_\mathrm{ff} = \left(\frac{R}{g_\mathrm{s}} \right)^{1/2} = \left(\frac{R^3}{GM} \right)^{1/2} \simeq 4000\,\mathrm{s}. \tag{8}$$

- *Kelvin–Helmholtz time-scale*. The thermal (or Kelvin–Helmholtz) time-scale measures the time it would take to empty the star of its thermal content, given its current luminosity

$$t_\mathrm{KH} = \frac{\rho c_\mathrm{p} T R^3}{L} \simeq 3 \times 10^{12}\,\mathrm{s}. \tag{9}$$

Table 1
Typical values for a 2.2 solar masses stellar model; T, P, and ρ are in the middle of the radiative region

Quantity	Typical value
ρ	$0.1\,\mathrm{g/cm^3}$
T	$3\times10^6\,\mathrm{K}$
s	$c_\mathrm{p}\simeq 3\times10^8\,\mathrm{erg/K/g}$
R	$1.5\times10^{11}\,\mathrm{cm}$
M	$4\times10^{33}\,\mathrm{g}$
L	$10^{35}\,\mathrm{erg/s}$
g	$g_\mathrm{s}=(GM/R^2)\simeq10^4\,\mathrm{cm/s^2}$
ν	$2\times10^2\,\mathrm{cm^2/s}$
χ	$2\times10^{16}\,\mathrm{erg/cm/K/s}$
P	$5\times10^{13}\,\mathrm{dyne}$
Ω	10^{-6}–$10^{-4}\,\mathrm{s}$

- *Eddington–Sweet time-scale*. The meridional circulation (or Eddington–Sweet) time-scale is calculated using the fraction of the thermal energy that is in imbalance (cf. [48]), namely

$$t_\mathrm{ES}=\frac{t_\mathrm{KH}}{\mathscr{A}}=\frac{t_\mathrm{KH}g_\mathrm{s}}{\Omega^2R}\simeq 3\times10^{13}\text{–}3\times10^{17}\,\mathrm{s} \tag{10}$$

  for the fastest and the slowest rotators, respectively (the oblateness $\mathscr{A}$ will be introduced in Section 2.3).
- *Nuclear time-scale*. This time-scale evaluates the duration of the main sequence, the central hydrogen burning (and longest) evolutionary stage. It is related to the energy released by converting ^{1}H to ^{4}He. That reaction releases $Q=6.3\times10^{18}\,\mathrm{erg/g}$ leading to

$$t_\mathrm{n}=\frac{E_\mathrm{n}}{L}=\frac{QM}{L}\simeq 5\times10^{18}\,\mathrm{s}. \tag{11}$$

- *Rotational time-scale*. The relevant time-scale is the rotational period

$$t_\mathrm{rot}=\frac{1}{\Omega}\simeq 10^4\text{–}10^6\,\mathrm{s}. \tag{12}$$

We observe the important hierarchy

$$t_\mathrm{n}\gg t_\mathrm{ES}\gg t_\mathrm{ff}. \tag{13}$$

It is thus possible to neglect nuclear transformations while studying the dynamics of large scale circulation. The case of pressure waves is however trickier, and will be discussed in the next section.

2.2. Anelastic approximation

Pressure waves are of fundamental importance in re-adjusting the system against perturbations. However, when using an explicit code as we shall be doing, the stability criterion requires that the time-step be small enough to describe those waves. In our case, this would severely constrain the numerics. Thus we need to consider a different system of equations in which the pressure waves are filtered out, and where the system is actually always "adjusted" against perturbations.

Several authors have performed formal developments of such an *anelastic approximation* [18,20,26,35], which may be heuristically understood as the result of using an infinite sound speed c_s in the mass equation. Indeed, we have (from Eq. (1))

$$\frac{\partial \rho}{\partial t} = \frac{1}{c_s^2}\frac{\partial P}{\partial t} = -\vec{\nabla}\cdot\left(\rho\vec{w}\right), \tag{14}$$

where we used $c_s^2 = \gamma P/\rho$ and $\gamma = \partial P/\partial\rho|_s$. Taking the divergence of a simplified momentum equation (cf. Eq. (2)) involving only the pressure forces

$$\frac{\partial}{\partial t}\vec{\nabla}\cdot\left(\rho\vec{w}\right) + \nabla^2 P = 0$$

and introducing it into the time derivative of (14) leads to the pressure wave equation

$$\frac{1}{c_s^2}\frac{\partial^2 P}{\partial t^2} = \nabla^2 P.$$

Formally, this approximation also involves the linearization of the equations about a reference state

$$\rho \to \rho_0 + \rho,$$

where ρ_0 refers to the reference profile and ρ, to the perturbation. In our case, the reference state will be a Roche model (see Section 4.3) which will also be used for pressure and temperature. In order to filter out pressure waves and limit the problem to the reference state, the mass conservation equation (1) is thus replaced by the *anelastic condition*

$$\vec{\nabla}\cdot\left(\rho_0\vec{w}\right) = 0.$$

One of the numerical challenges will be to ensure that the latter condition is satisfied everywhere in the interior at all times (see Section 2.4).

Pressure waves are not the only physical processes occurring on a dynamical time-scale. Several dynamical instabilities, like shear instabilities for example, occur on similar time-scales. We will describe their treatment in the following section.

2.3. Dimensionless equations

The next step is to write dimensionless equations. We chose the dimensions given in Table 2, based on the use of a dynamical velocity.

Table 2
Scaling and characteristic numbers

w	$\to$	$(R/t_{\mathrm{ff}})w$
r	$\to$	Rr
t	$\to$	$t_{\mathrm{ff}}t$
g	$\to$	$(GM/R^2)g$
s	$\to$	$c_p s$
ρ	$\to$	$\rho^*\rho$
P	$\to$	$\rho^*(GM/R)P$
T	$\to$	$(GM/R)(\mu/\mathscr{R})T = T^*T$
v	$\to$	v^*v
χ	$\to$	$(L/(4\pi RT^*))\chi$
$(\Omega^2R^3)/GM$	$\to$	$\mathscr{A}$
$(GM/R)^{1/2}(R/\nu^*)$	$\to$	$\mathscr{R}e$

This scaling leads to the system of equations

$$\vec{\nabla}\cdot\left(\rho_0\vec{w}\right)=0, \tag{15}$$

$$\frac{\partial(\rho_0\vec{w})}{\partial t}+\vec{\nabla}\cdot\left(\rho_0\vec{w}\vec{w}+P\bar{\bar{I}}-\frac{1}{\mathscr{R}e}\bar{\bar{\tau}}\right)=\rho\vec{g}_{\mathrm{eff}}-\mathscr{A}^{1/2}\rho_0\vec{e}_z\times\vec{w}, \tag{16}$$

$$\rho_0 T_0\frac{\partial s}{\partial t}+\rho_0 T_0\vec{\nabla}s\cdot\vec{w}=\left(\frac{v^*}{T^* c_{\mathrm{p}} t_{\mathrm{ff}}}\bar{\bar{\tau}}\cdot\vec{\nabla}\right)\vec{w}+\frac{t_{\mathrm{ff}}}{t_{\mathrm{KH}}}\vec{\nabla}\cdot\left(\chi\vec{\nabla}[T_0+T]\right), \tag{17}$$

where $\vec{g}_{\mathrm{eff}}=g(\vec{e}_r+\mathscr{A}\varpi\vec{e}_\varpi)$, $\varpi^2=x^2+y^2$, and $\varpi\vec{e}_\varpi=(x\vec{e}_x+y\vec{e}_y)$. In these equations, we also introduced non-dimensional numbers characterizing the problem, like the oblateness $\mathscr{A}$ which measures the ratio of centrifugal force to gravity and the Reynolds number, $\mathscr{R}e$, characterizing the viscosity in comparison to the scaling velocity and length scale.

Once the equations are put in a dimensionless form using dynamical (cf. Eq. (8)) and thermal (cf. Eq. (9)) time-scales, we will lengthen the dynamical time-scale in order to be able to simulate both thermal and dynamical instabilities at the same time. This is done by increasing the ratio $t_{\mathrm{ff}}/t_{\mathrm{KH}}$ in the heat equation (17) and actually corresponds to increasing the star's luminosity. This will enhance meridional circulation as well as its corresponding differential rotation.

2.4. Pressure perturbation

In our system of equations, we replaced a prognostic (i.e.time-dependent) equation expressing mass conservation by a diagnostic (i.e., time-independent) equation, the anelastic condition. It is an important numerical problem to ensure that this condition is satisfied everywhere in the fluid. That is done through the calculation of pressure via a Poisson equation, obtained by combining the divergence of the momentum equation (16) with the anelastic condition (15). Thus we evaluate the pressure field that will allow the non-divergence of momentum to be preserved

$$\nabla^2 P=-\partial_i\partial_j\left(\rho_0 w_i w_j\right)+\frac{v}{\mathscr{R}e}\partial_i\partial_j\tau_{ij}+\partial_i(\rho g_{\mathrm{eff}} i)+\mathscr{A}^{1/2}\left[\partial_x\left(\rho_0 w_y\right)-\partial_y(\rho_0 w_x)\right]. \tag{18}$$

That equation is solved using a Jacobi method [40] combined with our fictitious point method for the boundary conditions (see Section 3). The basic idea behind Jacobi type methods consists in replacing the elliptic problem

$$\nabla^2 P=q \tag{19}$$

by a pseudo-time (ζ) dependent problem

$$\frac{\partial P}{\partial\zeta}=\nabla^2 P-q. \tag{20}$$

When convergence to a constant pressure field is reached, the elliptic problem (19) is solved. In the Jacobi method, the equation is treated explicitly and the selected time-step is the maximum stable step size as given by the CFL condition.

A number of methods have been tried but found less desirable than the Jacobi method. The Gauss–Seidel method,[1] which theoretically converges about twice as rapidly as the former [40], is inappropriate in

[1] In the Gauss–Seidel method, values of P are updated in the r.h.s. calculation as soon as they are available.

our problem for two reasons. Firstly, it does not preserve inherent symmetries. Secondly, due to the irregularity of the boundaries, boundary values depend on each other (see Section 3 for more details); if they are updated only at the end of the loop over grid points, our tests show that the Gauss–Seidel method then converges *more slowly* than the Jacobi method. On the other hand, calculating boundary values within the spatial loop impedes efficient parallelization.

Another scheme which could be used is the "odd–even" separation of the loops,[2] with "in place" updating, as in the Gauss–Seidel method. This method has the same theoretical convergence as the Gauss–Seidel algorithm, but does preserve symmetries. However, to obtain this rapid convergence, boundary conditions must be applied after each of the eight separate loops; since the tri-linear interpolations involved in the computation of the boundary conditions on the fictitious domain are rather time consuming (see below), that method will be more efficient than the Jacobi algorithm only below a certain surface/volume ratio, corresponding to a rather large problem ($\gtrsim 512^3$ grid points for our stellar case).

Finally, even though the Jacobi method is known to converge rather slowly [40], since pressure is updated at each time-step, it is expected that relatively few (pseudo-time) iterations will be needed, considering that the density and velocity fields evolve slowly with time.

The Poisson equation can also be solved more rapidly using FFTs (see e.g. [27]). However, such a treatment amplifies the importance of the privileged directions along the x, y, and z axes, and, even for the laminar flows we are testing here, axial symmetry would be lost (see Fig. 7).

3. The stars surface as an internal boundary

Several authors have discussed the advantage of using a regular Cartesian grid to perform numerical simulations involving irregular geometries (see [32]). Equations are then easily discretized, in a way which is problem independent. However, one then has to make the system of equations compliant with complex boundaries.

In many cases, the boundary conditions used are of "no flux" type. The problem is then dealt with by imposing a different volume and center of mass to boundary cells (see e.g., the recent contribution of Calhoun and LeVeque [6]).

In the present numerical simulation however, we must be able to apply a variety of boundary conditions. We first discuss the boundary condition for pressure (Section 3.1) and then, for the velocity field (Section 3.2).

3.1. Neumann or Dirichlet boundary condition

On the Poisson equation, we want to apply the Neumann condition ($\partial_{\vec{n}} P = 0$). In order to perform that calculation, one must first locate the position of the surface (squares in Fig. 1) and determine its normal. In our fictitious point approach, we first identify all points that are *inside* the star (filled circles in Fig. 1). Then, to each boundary point (open circles), we associate a fictitious point (for a typical 64^3 simulation, the fictitious points are shown in Fig. 2), which is the boundary point's normal projection (defined by $\vec{\nabla}\Phi$) on the surface equipotential (see Section 4.3). The value of the physical variable at the grid point is then calculated using a tri-linear, $\mathcal{O}(\delta x^1)$, interpolation so that the desired condition is satisfied at the corresponding fictitious point. Since such an interpolation may require the use of other points which are actually outside the star, care must be taken to perform the interpolations in the correct sequence (see Figs. 1 and 3).

[2] Here, the single 3D-spatial loop is replaced by eight loops, odd and even points in each direction being treated separately.

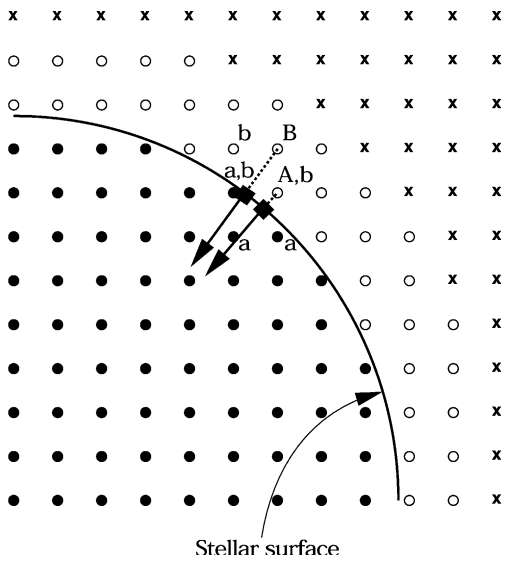

Fig. 1. Illustration of the concept of fictitious points. Filled circles are in the stellar interior while open ones are the boundary points, calculated via a tri-linear (in 3D) interpolation to comply with the required boundary conditions at the fictitious points on the star's surface (squares). Crosses are not used. Point A is calculated using points labeled a and point B, those labeled b. Note that some of these points are themselves boundary points and need to be calculated before point B.

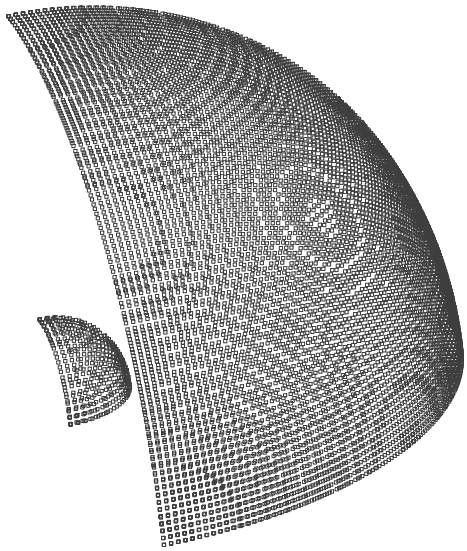

Fig. 2. Fictitious points used for the 64^3 simulation.

3.1.1. A test case: solving the Poisson equation

As a test of the fictitious point method, we first solve the equation

$$\nabla^2 P = q = \nabla^2(\cos r) = -\frac{2}{r}\sin r - \cos r \tag{21}$$

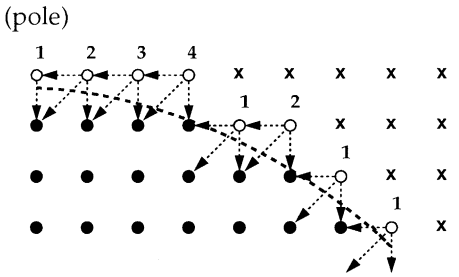

Fig. 3. Illustration of the importance of the order of bi-linear interpolations. Border point numbers illustrate the order in which the interpolations must proceed while the arrows indicates the 3 points used for the interpolation.

in a hollow sphere with $r \in [\pi, 4\pi]$ and homogeneous Neumann condition, and then

$$\nabla^2 P = q = \nabla^2(\sin r) = \frac{2}{r}\cos r - \sin r \tag{22}$$

over the same domain but this time with homogeneous Dirichlet boundary condition. For both problems, the fictitious point method (hereafter FP) is compared to a simple "staircase" method, in which boundary conditions are applied to the irregular boundary with no interpolation, as would be done on a regular domain. The initial condition is taken to be $\xi \times \cos r$ in the first simulation (or $\xi \times \sin r$ in the second simulation) where ξ is a random real number $\in [0, 1]$ changing at each grid point.

Fig. 4 shows the evolution of the mean error $\langle e \rangle$

$$\langle e \rangle = \frac{1}{N}\sum_{i=1}^{N} \left| P_i^{\text{exact}} - P_i^{\text{num}} \right|, \tag{23}$$

where N is the number of points inside the hollow sphere. Results are for 64^3 grid points. This graph shows that the use of the fictitious point method leads to smaller errors than the staircase method. Furthermore, the mean error $\langle e \rangle$ then remains closer to its minimum value as iterations are performed beyond the optimal number of steps leading to $\langle e \rangle = \langle e \rangle_{\min}$.

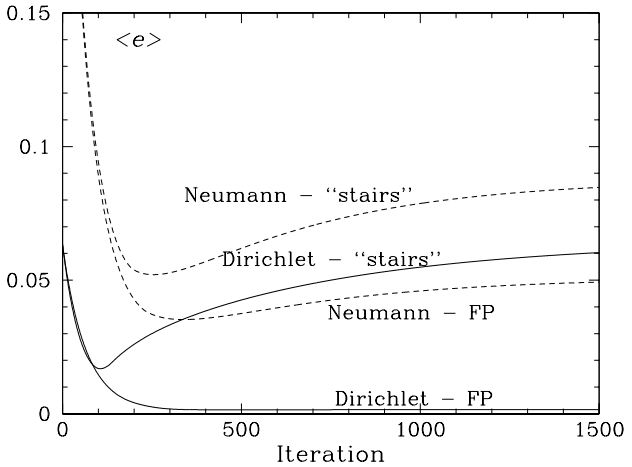

Fig. 4. Evolution of the mean error (Eq. (23)) for two different boundary conditions, Dirichlet and Neumann, and two different methods, the fictitious points method (FP) and the "staircase" method.

Fig. 5 shows the resulting profile at the equator corresponding to the minimum error (i.e., the smallest mean error as defined by Eq. (23)) in all four cases. The larger error in the case of the Neumann condition can be attributed to the fact that the Poisson equation involves only second derivatives of the unknown function. The Dirichlet boundary condition completely defines the solution, whereas the Neumann condition defines it only up to a constant, thus leading to a larger error on the absolute value. In this numerical example, the constant was fixed by forcing the pressure to have zero mean. In the physical problem, it is the pressure gradient that is required for the momentum equation; however, via the equation of state, the pressure's amplitude will change the density, and we thus adjust the additive constant to conserve mass. The fact that the boundary condition is applied only at $\mathcal{O}(\delta x^1)$ as is done usually to damp oscillations [37] tends to smooth the border too rapidly, thus causing a larger absolute error. Fig. 6 shows the evolution of the minimum error in all four cases as a function of resolution. The error on the FP-Dirichlet solution decays at $\mathcal{O}(\delta x^2)$, as expected for the standard Jacobi method, even though the boundary condition is applied at $\mathcal{O}(\delta x^1)$. It is not the case however for the FP-Neumann solution, nor for both "stairs" solutions, which converge at $\mathcal{O}(\delta x^1)$.

Another important property is the influence of the boundary condition on the symmetry of the solution. Indeed, the grid contains preferred transport directions, which leads to some limitations in the use of Cartesian methods (for example, the azimuthal component cannot be described accurately in 64^3 if its magnitude is less than about a tenth of the meridional components). The boundary conditions will also influence the solution's symmetry, and must be introduced so as to minimize their impact. In Fig. 7, we give a measure of the resultant symmetry by comparing the azimuthal average of the pressure field and its value in the $\phi = 0$ plane. We define a root mean square deviation σ

$$\sigma = \left\{ \frac{1}{N} \sum_{i=1}^{N} \left[P(r,\theta,\phi)_{\phi} - P(r,\theta,0) \right]^2 \right\}^{1/2}, \tag{24}$$

where the sum is made on all (N) interior point, and r, θ, ϕ are the spherical coordinates. The advantage of the fictitious point method for the Neumann condition is more obvious here.

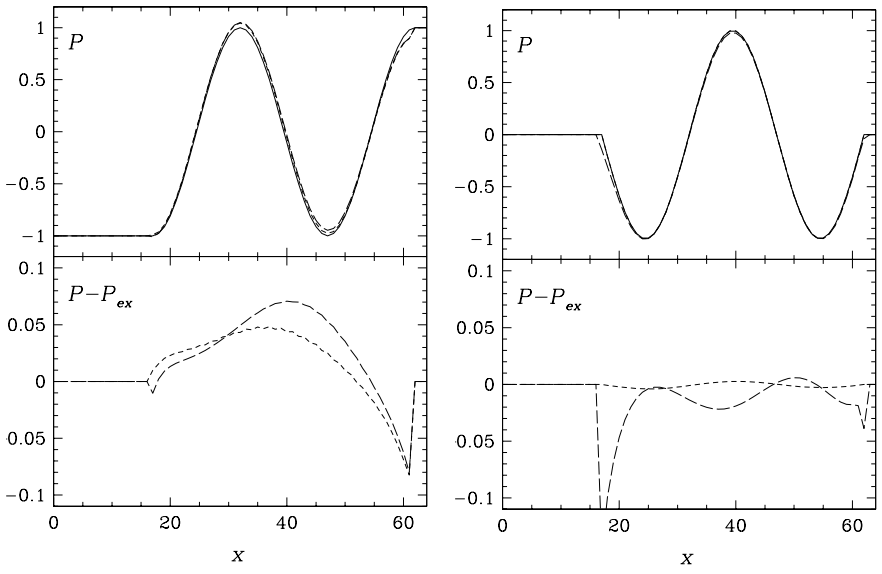

Fig. 5. Solution profile corresponding to the smallest error; left: Neumann boundary condition; right: Dirichlet boundary condition; top: solution; bottom: error. The solid line is the exact function, the dashed line is the FP solution and the long-dashed line the "stairs" solution.

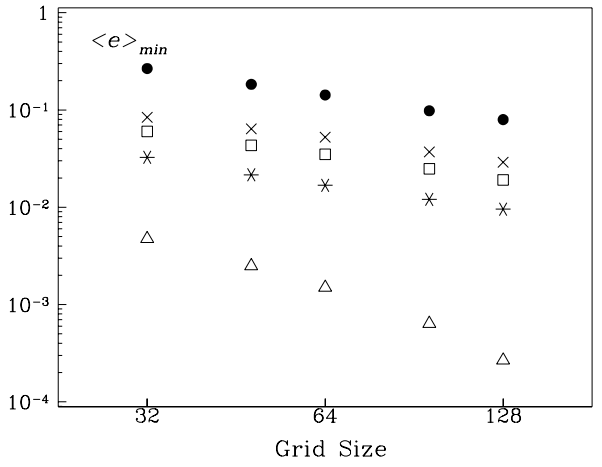

Fig. 6. Minimum mean error at various resolution. Crosses are for "stairs"-Neumann, squares for FP-Neumann, stars for "stairs"-Dirichlet, and triangles for FP-Dirichlet. Dots are results obtained via FFTs for the Neumann condition.

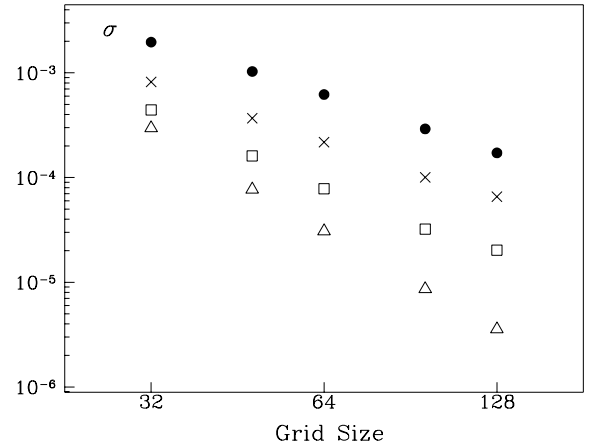

Fig. 7. Root mean square deviation between the solution's azimuthal average and the $\phi = 0$ plane value (Eq. (24)). Crosses are for the staircase solution and squares for the FP case. Triangles are the values obtained when the exact value is used on grid points, giving a measure of the part of the error due to the linear interpolations performed in the calculation of σ. Dots are results obtained via FFTs.

3.1.2. A multi-grid approach?

The Jacobi and other related methods on Cartesian meshes can be sped up by using multi-grid algorithms in which lower resolution grids are used alternately with higher resolution ones (see e.g. [10]). Convergence is then much faster unless small scale structure is clearly dominant.

In our problem with fictitious points however, that method is not straightforward. Indeed, the ability to apply the boundary condition at each iteration is of great importance in the convergence process. Contrarily to the case of a rectangular domain in which boundary cells do not change in the multi-grid process (provided the resolution is properly chosen), in our stellar problem with ellipsoidal geometry they change for each grid.

Since after some tests they were found to give quite unsatisfactory results, multi-grid methods will not be further discussed here.

3.2. Stress-free boundary conditions

As already mentioned, boundary conditions on the velocity field $\vec{w}$ must be applied at the star's surface. The first condition is that the normal component must vanish on the star's surface

$$\vec{w} \cdot \vec{n} = 0, \tag{25}$$

where $\vec{n}$ is the normal vector. One must also apply the so-called stress-free boundary condition [50] which states that the normal component of the stress-tensor must vanish or

$$(\vec{n} \cdot \bar{\bar{\tau}}) \cdot \vec{t}_i = 0, \tag{26}$$

where $\vec{t}_i$ denotes any vector tangential to the surface. Selecting two perpendicular vectors suffices to ensure that this condition is satisfied for any tangential vector.[3] Taking (25) into account, (26) is equivalent to

$$\partial_{\vec{n}}\left(\vec{w} \cdot \vec{t}_i\right) = 0, \tag{27}$$

where $\partial_{\vec{n}}$ denotes the normal derivative. Eq. (25) together with (27) for $i = 1, 2$ leads to three equations, for the three components of the velocity field.

Tests of the validity of the approach will be presented with the preliminary results (Section 5).

4. Finite volume discretization and program algorithm

In our Navier–Stokes solver we consider that only the perturbations, which are assumed small, change with time. The time-dependent parts of equations (16) and (17) are then discretized using a cell-centered finite volume method [22]. In this method, the evolution of the average value over a control volume $\mathscr{V}$ of a quantity x is calculated using its flux integrated over the bounding surface $\mathscr{S}$ of $\mathscr{V}$, plus its volume variation integrated over $\mathscr{V}$ (see Fig. 8). We get the system of equations

$$\int_{\mathscr{V}} \frac{\partial(\rho_0 \vec{w})}{\partial t}\,\mathrm{d}\mathscr{V} = \int_{\mathscr{S}} -\left(\rho_0 \vec{w}\vec{w} + P\bar{\bar{I}} - \frac{v}{\mathscr{R}e}\bar{\bar{\tau}}\right) \cdot \mathrm{d}\vec{\mathscr{S}} + \int_{\mathscr{V}} \left(\rho \vec{g}_{\mathrm{eff}} - \mathscr{A}^{1/2}\rho_0 \vec{e}_z \times \vec{w}\right)\mathrm{d}\mathscr{V}, \tag{28}$$

$$\int_{\mathscr{V}} \rho_0 \frac{\partial s}{\partial t}\mathrm{d}\mathscr{V} = \int_{\mathscr{S}} -\rho_0[s_0 + s]\vec{w} \cdot \mathrm{d}\vec{\mathscr{S}} + \frac{1}{\langle T_0 \rangle}\frac{t_{\mathrm{ff}}}{t_{\mathrm{KH}}}\int_{\mathscr{S}} \chi\vec{\nabla}[T_0 + T] \cdot \mathrm{d}\vec{\mathscr{S}} + \frac{1}{\langle T_0 \rangle}\frac{v^*}{T^* c_{\mathrm{p}} t_{\mathrm{ff}}}\int_{\mathscr{V}} \left(\bar{\bar{\tau}} \cdot \vec{\nabla}\right) \cdot \vec{w}\,\mathrm{d}\mathscr{V}. \tag{29}$$

The advantage of the finite volume method is that we are dealing directly with the fluxes at the cell interfaces thus ensuring conservation of the relevant physical quantities. We are dealing with two "spaces," which we call the *volume space*, in which the average values are given, and the *mesh space*, for those on the mesh points (cf. Fig. 8). The volume space is the one in which equations are solved, while fluxes are calculated and boundary conditions applied in the mesh space.

4.1. From volume to mesh space: reconstruction

The transformation from volume to mesh space is done by using the definition of integrals and derivatives. The concept is easy to illustrate with a 1D example [22,28]. Assuming that the volume (or mean)

[3] In order to further reduce the importance of preferred directions, we choose the first tangential vector $\vec{t}_1$ along a meridional plane, the second being just $\vec{t}_2 = \vec{t}_1 \times \vec{n}$.

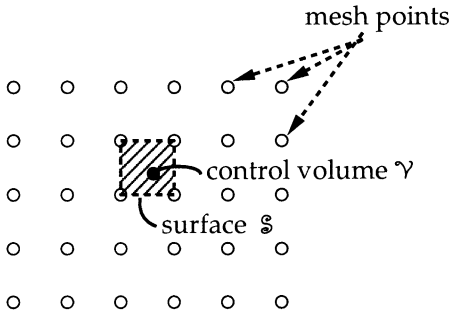

Fig. 8. Illustration of mesh points, of a control volume (hatched) and its surface (dotted line) in 2D.

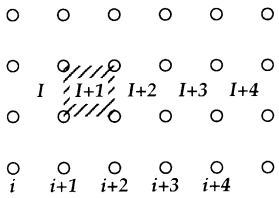

Fig. 9. Numbering control volumes ("I") and mesh points ("i") in 2D.

value of some variable f within each cell is known exactly, one can evaluate the *exact* integral at the mesh points

$$\int_0^{x_i} f\,\mathrm{d}x = \sum_{I=0}^{i-1} F_I \Delta x, \tag{30}$$

where volume values are designated with capital letters and mesh values with small ones (see also Fig. 9). This is called reconstruction via primitive variables [28]. Then, the mesh value is given by the derivative of the integral

$$f_i = \frac{\mathrm{d}}{\mathrm{d}x}\left[\int f\,\mathrm{d}x\right]_i = \frac{\mathrm{d}}{\mathrm{d}x}\left[\sum F_I \Delta x\right]_i, \tag{31}$$

which can be evaluated using a finite difference approach of desired accuracy.

4.2. From mesh to volume space: averaging

The opposite transformation consists of calculating the volume value from those on the mesh. One must first compute the interpolating polynomial (of a given accuracy) fitting the mesh points and then, calculate the analytic integral of that polynomial. A second-order approach leads to the simple expression

$$F_I = \frac{1}{2}(f_i + f_{i+1}) \tag{32}$$

while a fourth-order formulation gives

$$F_I = \frac{1}{14}(-f_{i-1} + 8f_i + 8f_{i+1} - f_{i+2}). \tag{33}$$

Going from 1D to 3D requires repeating the procedure once in each direction.

4.3. Reference state

In our problem, the anelastic approximation requires the use of a reference profile [20], variable x being expressed as the sum of a mean value x_0 plus a perturbation x.

We chose as reference state a "point mass star"[4] in solid body rotation. The equipotential Φ is then given by the Roche potential (see e.g. [24])

$$\Phi = H\left(\frac{1}{r} + \mathscr{A}\varpi^2\right), \tag{34}$$

where H is a constant fixed by the requirement to reproduce gravity. The stellar structure equations

$$\frac{1}{\rho_0}\vec{\nabla}P_0 = \vec{\nabla}\Phi = \vec{g}_{\text{eff}} \quad \text{and} \quad \chi\vec{\nabla}T_0 = L\vec{n}, \tag{35}$$

where $\vec{n}$ is the unit vector perpendicular to the local equipotential, are then solved for the barotropic model. In such a model, the divergence of the heat flux is non-zero, giving rise to meridional circulation. This divergence is computed using an analytical formulation valid for solid body rotation and in the point mass star approximation. In non-dimensional units, we get (cf. [21,36,48])

$$\vec{\nabla}\cdot\left(\chi\vec{\nabla}T_0\right) = \frac{t_{\text{ff}}}{t_{\text{KH}}}2\rho_0 r^3\frac{R^3}{\rho^* M}\frac{\widetilde{g}}{g}P_2(\cos\theta) = \frac{t_{\text{ff}}}{t_{\text{KH}}}\frac{8\rho_0 r^3}{3}\frac{R^3}{\rho^* M}\mathscr{A}P_2(\cos\theta), \tag{36}$$

where $P_2(\cos\theta)$ is a Legendre polynomial and $(\widetilde{g}/g)P_2(\cos\theta)$ represents the latitudinal gravity fluctuation on the equipotential.

4.4. Algorithm

We then deal with the evaluation of the volume value of selected variables, namely the entropy s and the velocity $\vec{w}$. We also include the transport of a non-reactive tracer to illustrate the circulation's cumulative effect. The time integration is done using an explicit second-order Adams–Bashforth scheme, for which the evolution of a quantity x is given with respect to the explicit net variation at two different time-steps

$$x^{t+\Delta t} - x^t = \Delta t\cdot\left(1.5\mathscr{F}^t - 0.5\mathscr{F}^{t-\Delta t}\right), \tag{37}$$

where $\mathscr{F}\Delta t$ expresses the net variation of a volume quantity within a cell, which is calculated using Eqs. (28) and (29).

The code's algorithm is as follows:

1. Construction of the reference model, corresponding to a uniformly rotating star (cf. Section 4.3), including calculation of the source term:

$$\frac{t_{\text{ff}}}{t_{\text{KH}}}\int_{\mathscr{V}}\vec{\nabla}\cdot\left(\chi\vec{\nabla}T_0\right)\mathrm{d}\mathscr{V} \tag{38}$$

   (this would be zero in a non-rotating star).
2. Localization of the surface, classification of points (inner points, border points, and exterior points), and calculation of the tri-linear interpolation coefficients on the fictitious points (cf. Section 3).
3. Initialization to zero of all perturbation variables.
4. Time loop

[4] In the "point mass star" approximation one assumes in defining the potential that the mass in concentrated at the center.

(a) Evaluate mesh values for entropy and velocity fields.
(b) Calculate corrections to the mesh velocity field to re-enforce the anelastic condition,[5] by solving an equation for a pressure correction ϕ

$$\nabla^2\phi = \frac{\vec{\nabla}\cdot\left(\rho_0\vec{w}\right)^*}{\delta t}. \tag{39}$$

The total pressure perturbation is then given by

$$P \to P + \phi, \tag{40}$$

and the momentum field becomes

$$\rho_0\overrightarrow{w_i} = \left(\rho_0\overrightarrow{w_i}\right)^* - \frac{\partial\phi}{\partial x_i}\delta t. \tag{41}$$

(c) Apply boundary conditions to mesh fields.
(d) Make a cell average using (33), to convey the boundary conditions and velocity corrections to the volume fields.
(e) Update the pressure perturbation, using (18), and the corresponding temperature and density fields, imposing mass conservation.
(f) Calculate the net variation $\mathscr{F}^t$ of entropy and velocity fields using (28) and (29).
(g) Update entropy and velocity fields using a second-order Adams–Bashforth scheme (cf. Eq. (37)).
(h) Output at given time-steps.

5. Validation of approach

We present results obtained with a test simulation using 64^3 points. We simulated 1/8th of the star, assuming symmetry about the equator and re-injecting the outgoing flow from the $y = 0$ plane (or in spherical coordinates the $\phi = 0$ plane) into the $x = 0$ plane. The exact parameters used for the simulation are given in Table 3. The shape of the star as well as the source term are realistic, while viscosity is greatly overestimated, and stratification is underestimated.

The key to meridional circulation is the source term, coming from the divergence of the radiative flux. It has been known for quite a long time that a star in solid rotation cannot achieve thermal equilibrium thus leading to sinks and sources of heat [58]. This source term is shown in Fig. 10 for our model star. In a realistic star covering several scale heights, close to the surface there would be a reversal of the sink and source. Gratton [21] and Öpik [36] have suggested this could lead to a reversed circulation cell. Such a feature cannot appear in this preliminary study, as it requires a higher resolution, a lower viscosity and a more pronounced stratification to resolve it numerically.

In this viscous simulation, an equilibrium state was reached after $\sim 4t_{\mathrm{KH}}$ starting from a fluid in solid body rotation and no meridional flow. The equilibrium characteristics are illustrated in Figs. 11–13. Fig. 11 shows the resulting circulation velocity, which here consists of only one large cell. One can notice that the velocities rising along the pole are larger than those sinking along the equator, as required by mass conservation. Meridional circulation has a "turn around" time-scale of $\sim 5t_{\mathrm{KH}}$ whereas the mean rotational period[6] is about $0.6t_{\mathrm{KH}}$.

[5] The pressure is calculated using the momentum at time $t - \delta t$ and, in general, the updated momentum field does not satisfy the anelastic condition. We thus "correct" the pressure and the momentum field accordingly (see e.g. [15]).
[6] In a realistic model, the dynamical (and hence rotational) time-scale would be much smaller.

Table 3
Parameters used in the simulation

Parameter	Value
$\mathscr{R}e$	10
$\mathscr{A}$	0.03
$t_{\rm ff}/t_{\rm KH}$	0.1
$P_{\rm bottom}/P_{\rm top}$	1.5

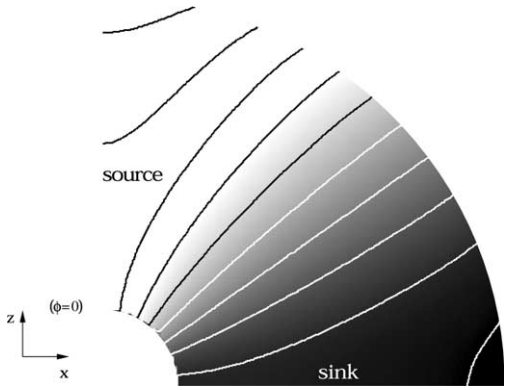

Fig. 10. Source term ($= \vec{\nabla} \cdot \vec{F}_{\rm radiative}$) of the meridional circulation used in the simulation. Light and dark areas have, respectively, positive and negative divergence.

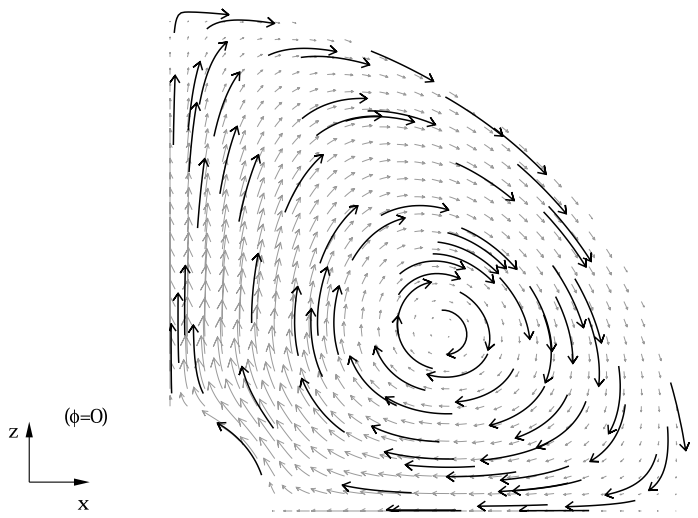

Fig. 11. Equilibrium circulation velocity. Black arrows are streamlines; the length of grey arrows is proportional to local velocity. Close to the center of the circulation cell, the period required to perform one complete revolution is $\sim 4t_{\rm KH}$, and it increases up to $\sim 11t_{\rm KH}$ in the outer part.

Fig. 12 illustrates the main contributions (integrated over one cell) to the equilibrium of the heat equation (29). On the r.h.s. of that equation, one has first the advection term (a), followed by the heat diffusion term, which here has been separated into the source term (b), corresponding to a barotropic star in

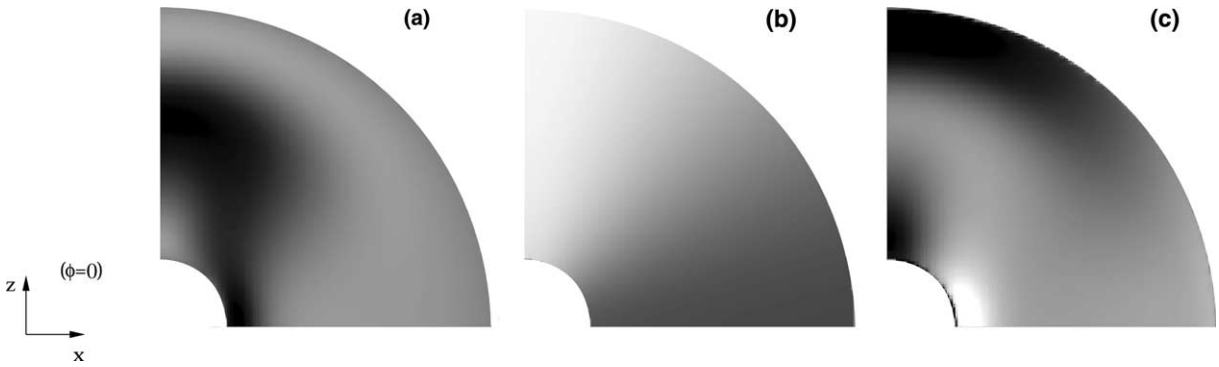

Fig. 12. Integrated contribution of various terms to the equilibrium heat flux in the $\phi = 0$ plane (cf. Eq. (29)). (a) Advection; (b) reference temperature; and (c) temperature perturbation (see text). White refers to positive and black to negative values.

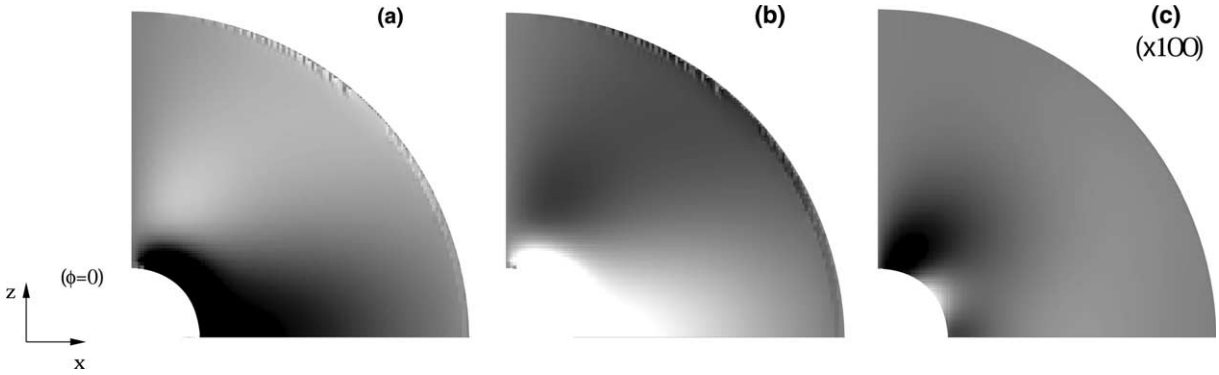

Fig. 13. Integrated contribution of major terms to the equilibrium x-momentum flux in the $\phi = 0$ plane (cf. Eq. (28)). (a) Gravity + pressure; (b) viscosity; (c) advection ($100\times$) (see text). White refers to positive and black to negative values.

solid body rotation, plus the contribution of the temperature perturbation (c). The last term represents heat generation related to viscosity and is much smaller than the previous ones in regimes relevant to the stellar case; it is not shown here.

In Fig. 13 we compare the contributions of various terms to the x-momentum equation (28). In the equilibrium state, the viscous transport (b, and 3rd r.h.s. of (28)) is balanced by a re-adjustment of the gravitational equilibrium (a and sum of 2nd and 4th r.h.s.). The advection term (c, 1st r.h.s.), next in magnitude, has been increased by 100 to be visible on this scale. The Coriolis term (5th r.h.s.) yields only a minor contribution to the final equilibrium reached in this simulation.

Finally, Fig. 14 shows the resulting differential rotation. Its magnitude is rather small, being about one hundredth of the meridional velocities, which is consistent with the large viscosities used in this preliminary simulation and with the fact that the Coriolis term does not contribute significantly to the equilibrium of Eq. (28). We expect this to change as viscosity is reduced to more realistic values. Indeed, a lower viscosity implies a larger differential rotation to get the same viscous transport. It could thus lead to the appearance of various dynamical instabilities (like e.g., the Kelvin–Helmholtz instability). The increase of stellar luminosity (or $t_{\mathrm{ff}}/t_{\mathrm{KH}}$) should help resolve both relevant time-scales simultaneously.

In Fig. 15, we show a comparison for the x component of the velocity field of the 64^3 and the 128^3 solutions. All fields correspond equally well at those two resolutions, an indication that we included enough spatial resolution for the problem, and that our numerical algorithm converges.

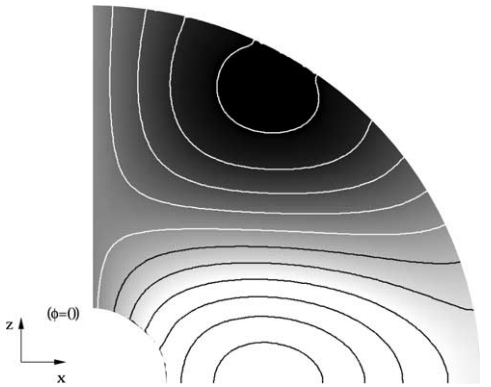

Fig. 14. Lines of constant azimuthal velocity (v_ϕ) in a meridional plane, corresponding to the equilibrium differential rotation in the star. Minimum and maximum values are $-9 \times 10^{-6} R/t_{\mathrm{KH}}$ and $4 \times 10^{-5} R/t_{\mathrm{KH}}$, respectively, and they are about two orders of magnitude smaller than the meridional components. White refers to positive and black to negative values.

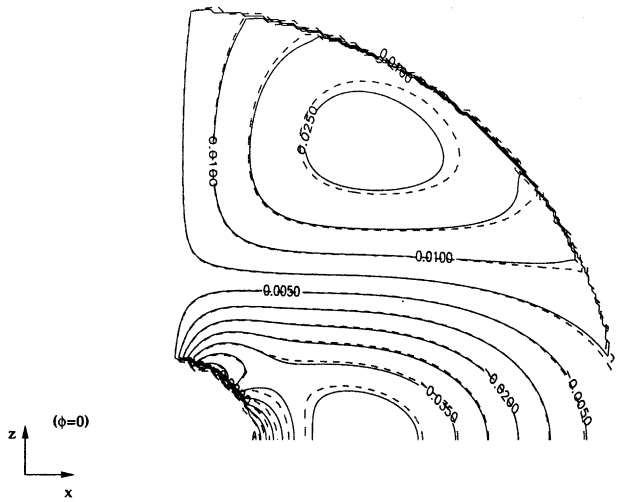

Fig. 15. Equilibrium x velocity field (v_x) in the $\phi = 0$ plane at two resolution (full line: 128^3, dashed line: 64^3). The good agreement between the two solutions is an indication that, for the considered parameters, the solution is resolved at 64^3.

As a test, we artificially increased the Coriolis force by 1000; the resulting pattern changes significantly (cf. Figs. 16 and 17). The main circulation cell is broken into two and streamlines become more cylindrical; that is the expected effect of the Coriolis force, as stated by the Taylor–Proudman theorem ($\partial v/\partial z = 0$, [55]). That theorem applies if the Rossby number ($\mathscr{R}o = F_{\mathrm{inertia}}/F_{\mathrm{Coriolis}}$) and the Ekman number ($\mathscr{E}k = F_{\mathrm{viscous}}/F_{\mathrm{Coriolis}}$) are small enough (cf. [2]), as well as the Froude number ($\mathscr{F}r = w^2/(gR)$).[7] Here, we have $\mathscr{R}o \sim 10^{-5}$ and $\mathscr{E}k \sim 10^{-2}$ everywhere in the domain, while we had $\mathscr{R}o \sim 10^2$ and $\mathscr{E}k \sim 10^5$ previously. The horizontal movements are favored by the Coriolis force, and the equilibrium differential rotation is

[7] When stratification is important, the Taylor–Proudman theorem is replaced by the thermal wind equilibrium $\dfrac{\partial v}{\partial z} = \dfrac{g}{2\Omega \sin\theta T} \vec{e_z} \times \vec{\nabla} T$.

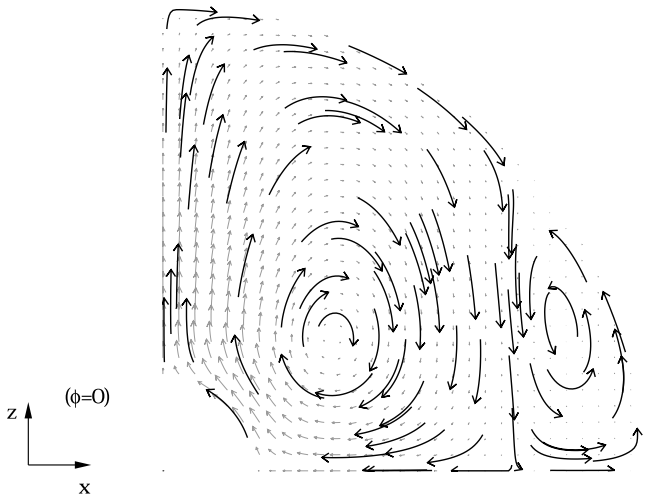

Fig. 16. Equilibrium circulation velocity when Coriolis acceleration is increased by 1000. Black arrows are streamlines; the length of grey arrows is proportional to local velocity. Circulation in the main cell is much faster then in the smaller outer cell. Periods to accomplish a complete revolution go from $\sim 8t_{\mathrm{KH}}$ to $\sim 55t_{\mathrm{KH}}$ towards the exterior of the main cell, while it ranges from $\sim 100t_{\mathrm{KH}}$ to $\sim 250t_{\mathrm{KH}}$ in the outer cell.

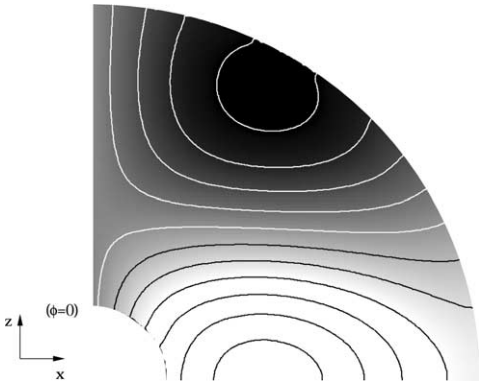

Fig. 17. Lines of constant azimuthal velocity (v_ϕ) in a meridional plane, corresponding to the equilibrium differential rotation in the star when Coriolis acceleration is increased by 1000. Minimum and maximum values are $-2.4 \times 10^{-3} R/t_{\mathrm{KH}}$ and $5 \times 10^{-3} R/t_{\mathrm{KH}}$, respectively, and they are about 50% larger than the meridional components. White refers to positive and black to negative values.

now larger than the meridional streaming. Smaller increases of the Coriolis force do enhance differential rotation, but do not produce splitting of the main cell (not shown). The final situation is characteristic of the geostrophic equilibrium in which the balance is between Coriolis acceleration and pressure fluctuations (see Fig. 18).

6. Discussion

In this paper, we presented the numerical approach developed to study the dynamics associated with meridional circulation in stars. We showed that our fictitious point method for boundary conditions yields

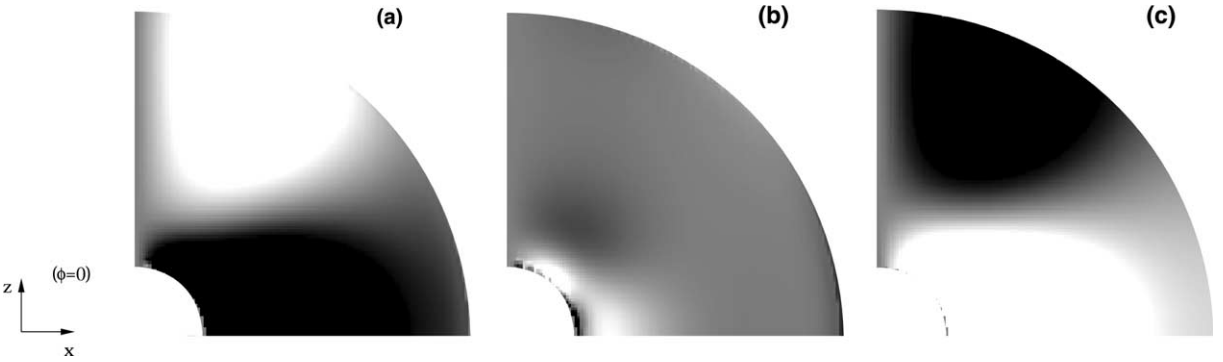

Fig. 18. Integrated contribution of major terms to the equilibrium x-momentum flux in the $\phi = 0$ plane (cf. Eq. (28)) when Coriolis acceleration is increased by 1000. (a) Gravity + pressure; (b) viscosity; (c) Coriolis (see text). White refers to positive and black to negative values.

satisfactory results in a test case of the Poisson equation, and presented preliminary results of large scale circulation.

We want to emphasize the advantage of using equally spaced Cartesian grids over the classical methods. The discrete set of equations obtained retains a simpler form than it would have in spherical coordinates, and we do not encounter small cells in the center of the grid. We also do not need to retain knowledge of the connectivity between cells, as one would in an un-structured grid. The main concern is that of producing flows that follow the imbedded surface properly, and this preliminary study confirms the correct behavior of the flows. Our results further show that we get good azimuthal symmetry given our choice of tangential vectors.

Another important property is the stability of the algorithm. In this test case, where a large viscosity is used, we find that the solution remains laminar at all times, and relaxes to the main circulation cell presented in Fig. 11 from any initial condition (as long as the CFL condition is not violated); there is no other stable equilibrium.

The next step is to come closer to conditions relevant for stellar evolution. We will first compare our results with those of theoretical models [51,53,62] in an appropriate regime. To do so, we must increase the stratification of the model and thus, the resolution. We can also assess the role of transients in the establishment of an equilibrium and study the effect of the circulation on the redistribution of chemicals.

Acknowledgements

S. Talon was supported by NSERC of Canada and by the Canada Research Chair in Stellar Astrophysics awarded to Gilles Fontaine. We would like to thank Michel Béland for his help in code vectorization and Maurice Meneguzzi who contributed to an early version of the code we are using. We thank the Réseau Québécois de Calcul de Haute Performance (RQCHP) for providing us with the computational resources required for this work.

References

[1] D.M. Anderson, G.B. McFadden, A.A. Wheeler, Diffuse-interface methods in fluid mechanics, Annu. Rev., Fluid Mech. 30 (1998) 139.
[2] P. Bartello, O. Métais, M. Lesieur, Coherent structures in three-dimensional turbulence, J. Fluid Mech. 273 (1994) 1.

[3] A. Brandenburg, K. Subramanian, Large scale dynamos with ambipolar diffusion nonlinearity, Astron. Astrophys. 361L (2000) 33.
[4] M. Briscolini, P. Santangelo, Development of the mask method for incompressible unsteady flows, J. Comput. Phys. 84 (1989) 57.
[5] M. Brüggen, W. Hillebrandt, Mixing through shear instabilities, Mon. Not. R. Astron. Soc. 320 (2001) 73.
[6] D. Calhoun, R.J. LeVeque, Solving the advection-diffusion equation in irregular geometries, J. Comput. Phys. 157 (2000) 143.
[7] P. Charbonneau, G. Michaud, Meridional circulation and diffusion in A and early F stars, Astrophys. J. 352 (1990) 681.
[8] C. Charbonnel, S. Talon, The hot side of the lithium dip – LiBeB abundances beyond the main sequence, Astron. Astrophys. 351 (1999) 635.
[9] M.J. Clement, Hydrodynamical simulations of rotating stars. I – a model for subgrid-scale flow, Astrophys. J. 406 (1993) 651.
[10] J. Demmel, UC Berkeley CS267 Applications of Parallel Computers lecture notes, 1996 http://www.cs.berkeley.edu:80/ demmel/cs267/lecture25/lecture25.html.
[11] R.G. Deupre, Two-dimensional hydrodynamic simulations of zero-age main-sequence convective cores, Astrophys. J. 543 (2000) 395.
[12] A.S. Eddington, Internal circulation in rotating stars, Observatory 48 (1925) 78.
[13] J.R. Elliott, Three-dimensional numerical simulations of compressible solar convection in Cartesian geometry, Astrophys. J. 539 (2000) 469.
[14] A.S. Endal, S. Sofia, The evolution of rotating stars. II – calculations with time-dependent redistribution of angular momentum for 7- and 10-solar-mass stars, Astrophys. J. 220 (1978) 279.
[15] J.H. Ferziger, M. Perić, Computational Methods for Fluid Dynamics, Springer, Berlin, 1996.
[16] K. Fricke, Instabilität stationärer Rotation in Sternen, Zeitschrift für Astrophysik 68 (1968) 317.
[17] P.A. Gilman, Nonlinear Boussinesq convective model for large scale solar circulations, Solar Phys. 27 (1972) 3.
[18] P.A. Gilman, G.A. Glatzmaier, Compressible convection in a rotating spherical shell. I – anelastic equations. II – a linear anelastic model. III – analytic model for compressible vorticity waves, Astrophys. J. Supplement 45 (1981) 335.
[19] P. Goldreich, G. Schubert, Differential rotation in stars, Astrophys. J. 150 (1967) 571.
[20] D.O. Gough, The anelastic approximation for thermal convection, J. Atmos. Sci. 26 (1969) 448.
[21] L. Gratton, Circolazione interna e instabilitá nelle binarie strette, Memorie della Societa Astronomia Italiana 17 (1945) 5.
[22] C. Hirsh, in: Numerical Computation of Internal and External Flows, vol. 1, Wiley, New York, 1988.
[23] R. Kippenhahn, Circulation and mixing, in: R.J. Tayler, J.E. Hesser (Eds.), IAU Symposium 66, Late Stages of Stellar Evolution, Reidel, Dordrecht, 1974.
[24] R. Kippenhahn, A. Weigert, Stellar Structure and Evolution, Springer, Berlin, 1990.
[25] E. Knobloch, H.C. Spruit, The molecular weight barrier and angular momentum transport in radiative stellar interiors, Astron. Astrophys. 125 (1983) 59.
[26] J. Latour, E.A. Spiegel, J. Toomre, J.-P. Zahn, Stellar convection theory. I. The anelastic modal equations, Astrophys. J. 207 (1976) 233.
[27] G. Lauritsch, P.-G. Reinhard, An FFT solver for the Coulomb problem, Int. J. Mod. Phys. C 5 (1994) 65.
[28] R.J. LeVeque, Computational Methods for Astrophysical Fluid Flow, Saas-Fee advanced course 27 lecture notes, 1997.
[29] A. Maeder, G. Meynet, The evolution of Rotating Stars, Annual Review Astron. Astrophys. 38 (2000) 143.
[30] A. Maeder, J.P. Zahn, Stellar evolution with rotation. III. Meridional circulation with μ-gradients and non-stationarity, Astron. Astrophys. 334 (1998) 1000.
[31] A. Malagoli, G. Bodo, R. Rosner, On the nonlinear evolution of magnetohydrodynamic Kelvin–Helmholtz instabilities, Astrophys. J. 456 (1996) 708.
[32] J.E. Melton, Automated three-dimensional Cartesian grid generation and Euler flow solutions for arbitrary geometries, Ph.D. thesis, UC Davis, June 1996 http://george.arc.nasa.gov/ jmelton/cartesian.html.
[33] L. Mestel, Rotation and stellar evolution, Mon. Not. R. Astron. Soc. 113 (1953) 716.
[34] M.S. Miesch, J.R. Elliott, J. Toomre, T.L. Clune, G.A. Glatzmaier, P.A. Gilman, Three-dimensional spherical simulations of solar convection. I. Differential rotation and pattern evolution achieved with laminar and turbulent states, Astrophys. J. 532 (2000) 593.
[35] Y. Ogura, N.A. Phillips, Scale analysis of deep and shallow convection in the atmosphere, J. Atmos. Sci. 19 (1962) 173.
[36] E.J. Öpik, Rotational currents, Mon. Not. R. Astron. Soc. 111 (1951) 278.
[37] T.J. Poinsot, S.K. Lele, Boundary conditions for direct simulations of compressible viscous flows, J. Comput. Phys. 101 (1992) 104.
[38] D. Porter, P.R. Woodward, Three-dimensional simulations of turbulent compressible convection, Astrophys. J. Supplement 127 (2000) 159.
[39] W.H. Press, Radiative and other effects from internal waves in solar and stellar interiors, Astrophys. J. 245 (1981) 286.
[40] W.H. Press, S.A. Teukolsky, W.T. Vetterling, B.P. Flannery, Numerical Recipes in C: The Art of Scientific Computing, Cambridge University Press, Cambridge, MA, 1992.
[41] Y. Osaki, Meridional circulation in a rotating star, Pub. Astron. Soc. Jpn. 24 (1972) 509.

[42] G. Randers, Large-scale motion in stars, Astrophys. J. 94 (1941) 109.
[43] O. Richard, G. Michaud, J. Richer, Iron convection zones, in B, A, and F stars, Astrophys. J. 558 (2001) 377.
[44] T. Sakurai, The evolution of the solar inner rotation, Mon. Not. R. Astron. Soc. 171 (1975) 35.
[45] E.A. Spiegel, J.P. Zahn, Instabilities of differential rotation, Comments Astrophys. Space Phys. 2 (1970) 178.
[46] E.A. Spiegel, A prelude to stellar convection theory, in: I.W. Roxburgh, J.L. Masnou (Eds.), Physical Processes in Astrophysics, Springer, Berlin, 1995.
[47] R.F. Stein, A. Nordlund, Simulations of solar granulation. I. General properties, Astrophys. J. 499 (1998) 914.
[48] P.A. Sweet, The importance of rotation in stellar evolution, Mon. Not. R. Astron. Soc. 110 (1950) 548.
[49] S. Talon, J.P. Zahn, A. Maeder, G. Meynet, Rotational mixing in early-type stars: the main-sequence evolution of a $9M_{\odot}$ star, Astron. Astrophys. 322 (1997) 209.
[50] J.L. Tassoul, Theory of Rotating Stars, Princeton University Press, Princeton, NJ, 1978.
[51] J.L. Tassoul, M. Tassoul, Meridional circulation in rotating stars. I – a boundary layer analysis of mean steady motions in early-type stars, Astrophys. J. Supplement 49 (1982) 317.
[52] J.L. Tassoul, M. Tassoul, Meridional circulation in rotating stars. IV – the approach to the mean steady state in early-type stars, Astrophys. J. 264 (1983) 298.
[53] M. Tassoul, J.L. Tassoul, Meridional circulation in rotating stars. XI – single-cell pattern versus double-cell pattern, Astrophys. J. 440 (1995) 789.
[54] J.-C. Thelen, F. Cattaneo, Dynamo action driven by convection: the influence of magnetic boundary conditions, Mon. Not. R. Astron. Soc. 315 (2000) L13.
[55] D.J. Tritton, in: Physical Fluid Dynamics, second ed., Oxford University Press, Oxford, 1988, pp. 217–226.
[56] S. Turcotte et al., Djehuty: A code for modeling whole stars in three dimensions, in: C. Aerts, T.R. Bedding, J. Christensen-Dalsgaard (Eds.), Radial and Nonradial Pulsations as Probes of Stellar Physics, ASP Conference Series, 2002.
[57] H.S. Udaykumar, R. Mittal, P. Rampunggoon, A. Khanna, A sharp interface Cartesian grid method for simulating flows with complex moving boundaries, J. Comput. Phys. 174 (2001) 345.
[58] H. vonZeipel, The radiative equilibrium of a rotating system of gaseous masses, Mon. Not. R. Astron. Soc. 84 (1924) 665.
[59] H. Vogt, Astron. Nachr. 223 (1925) 229.
[60] T. Ye, R. Mittal, H.S. Udaykumar, W. Shyy, An accurate Cartesian grid method for viscous incompressible flows with complex immersed boundaries, J. Comput. Phys. 156 (1999) 209.
[61] J.P. Zahn, Differential rotation and turbulence in stars, Mém. Soc. Roy. Sci. Liège 6e (série 8) (1975) 31.
[62] J.P. Zahn, Circulation and turbulence in rotating stars, Astron. Astrophys. 265 (1992) 115.